Chapter 4

Fabrication and Electrochemical Performance of Pseudocapacitive ABO_2-type Asymmetric cell $AgFeO_2$@C||$K_{0.4}MnO_2$. xH_2O for Large-scale Energy Storage Applications

In this chapter, crystallites of $K_{0.4}MnO_2$. xH_2O were successfully grown via a facile chemical flux method that gives a birnessite-type layered structure having a lateral dimension in the range of 2-5 µm. The incorporation of birnessite- $K_{0.4}MnO_2$. xH_2O as a positive electrode (cathode), and the thin carbon layer coated $AgFeO_2$ as a negative electrode (anode), in the form of an asymmetric cell (ASC), $AgFeO_2$@C//$K_{0.4}MnO_2$. xH_2O exhibited high energy density as well as power density with excellent cycle life up to cell voltages close to 1.8 V in 1M Na_2SO_4 electrolyte. The presented battery-type supercapacitor cell can deliver a maximum energy density equivalent to 61.51 Wh kg^{-1} and a power density of 450 W kg^{-1} at a current density of 0.5 A g^{-1}, which is substantially larger than the previously reported aqueous electrolyte-based asymmetric supercapacitor devices and can replace currently market available hazardous lead-acid batteries for fast energy storage applications.

4.1 Introduction

The ever-increasing demand for sustainable energy supply forced the electrochemists and material scientists to develop a highly efficient large-scale energy storage solution that can fill the gap between batteries (high energy density) and capacitors (high power density) [74][76][174]. Among various existing energy storage technologies, electrochemical energy storage systems (EESs) such as supercapacitors have received tremendous attention due to their unique property of fast charging/discharging and super-long lifetime. However, its low energy density needs to be addressed before utilizing it for grid-level energy storage solutions. The specific energy (E) of a supercapacitor can be increased either by improving the specific capacitance (C) of the electrode materials or by extending the cell voltage. Theoretically, the operating voltage window of an aqueous-based supercapacitor device is 1.23 V, however, a higher cell voltage can be achieved by fabricating an asymmetric cell (ASC) in which both, the positive and negative electrodes are worked in a separate potential window [175][176]. The operating cell voltages of previous existing aqueous-based ASCs mainly lie in the range of 1.4–2.0 V, depending upon the coupling of positive and negative electrode materials that possess large oxygen evolution overpotential and hydrogen evolution overpotential, respectively [177]–[184]. Therefore, developing a suitable cathode (positive) material in combination with a matching counter electrode, anode (negative) that exhibited comparable specific capacitances in the separate potential windows is a quite challenging and hot topic for the research to enhance the energy density of the ASC.

Among all the available cathode materials, MnO_2 has attracted great attention due to its large theoretical specific capacitance (1370 F g^{-1}), low cost, non-toxicity, and high oxygen evolution potential (potential window is about 1 V)[185][186]in the aqueous medium. However, due to the insufficient active sites and poor electronic conductivity (10^{-5} to 10^{-6} S cm^{-1}), MnO_2 can attain only 10 to 20% of its theoretical limit. Therefore, various strategies have been adopted to improve the electrochemical performance of MnO_2 that includes nanostructured designing, nanocomposite formation, foreign ion doping, etc. [187][188]. Recently, the charge storage performance of MnO_2 can be improved by pre-intercalation of cations such as Zn^+, K^+, and Na^+, etc., which resulted in the widening of the operational

potential window to get full access to Mn^{3+}/Mn^{4+} redox couple [189]. Additionally, pre-insertion of alkali ions can also increase the inter-layer separation of [MnO_6]-octahedral to reduce the diffusion path length of electrolyte ions, hence, increasing the specific capacitances of the MnO_2 electrode[190].

In the search for anode materials; carbon and its derivatives such as activated carbon, carbon nanotube, and graphene are widely used because of their high specific surface area, non-toxicity, and large overpotential for hydrogen evolution in aqueous neutral electrolytes [191]. However, in terms of specific capacitance, carbon cannot match well with MnO_2 electrodes, which will seriously limit the energy density of ASCs. Among the widely explored anode materials, iron oxides/hydroxides are the excellent choice because of their rich redox chemistry (Fe^0/Fe^{2+}, Fe^0/Fe^{3+}, Fe^{2+}/Fe^{3+}, Fe^{3+}/Fe^{4+}), low toxicity, and most earth-abundance [163][192][193]. The key challenge with current iron-based electrodes for supercapacitors is their poor electrochemical and cycling performance. Therefore, some effective approaches such as nanostructural design [167], selective ion substitution to form solid solutions [194], and protection of carbon layer have been employed to get rid of the above limitations of iron-based materials.

In the present study, we have fabricated an aqueous asymmetric cell in which, birnessite-$K_{0.4}MnO_2$. xH_2O acts as a positive electrode and thin carbon-coated $AgFeO_2$ as a negative electrode, which can be operated reversibly up to 1.8 V in a neutral 1M Na_2SO_4 electrolyte. The fabricated, $AgFeO_2$@C//$K_{0.4}MnO_2$. xH_2O battery-type supercapacitive ASC exhibited a specific capacitance of 136.69 F g^{-1} and energy density of 61.51 Wh kg^{-1} with a power density of 450 W kg^{-1} at a current density of 0.5 A g^{-1}, which is substantially larger than the previously reported aqueous based asymmetric supercapacitor devices.

4.2 Experimental

4.2.1 Synthesis of active material

Crystallites of layered potassium manganese oxide, $K_{0.4}MnO_2$. xH_2O, with birnessite-type structures, were successfully grown using the chemical flux method. KNO_3 (Qualigenes, 98%) and Mn_2O_3 (Sigma-Aldrich, 99%) were used as precursor compounds, here, KNO_3 also served as a fluxing agent. The starting materials, KNO_3 (12.3 g) and Mn_2O_3

(2.0 g) were mixed in the molar ratio of K: Mn to 1:5 using mortar and pestle and kept in a platinum crucible. The mixed compound was heated at 700 °C for 24 h and was gradually cooled to 300 °C at a rate of 10 K/h followed by natural cooling to room temperature. The crucible was covered with a lid during the entire heat treatment. The sample was recovered by washing it several times with double distilled water and dried overnight at 80 °C. The prepared material was black in color and was stored under an inert atmosphere for further characterization.

The $AgFeO_2$ nanoparticles were synthesized as previously reported procedure with slight modification. Typically, 0.01 M of silver nitrate ($AgNO_3$, 99.9%, HIMEDIA) and 0.01 M of iron nitrate ($Fe(NO_3)_3.9H_2O$, 98%, Merck) were dissolved in 100 ml of double distilled water. For the complete precipitation, 20 ml of 4 M NaOH solution was added dropwise in the above solution and allowed to stand for 3 hrs. The filtrate was collected and dried overnight at 80 °C. The carbon coating was performed by dispersing the $AgFeO_2$ nanoparticles in 0.02 M glucose aqueous solution for 48 h with subsequent annealing at 400 °C for 3 h in Ar-atmosphere. The resulting material ($AgFeO_2$@C) was black in color and used for further analysis without any preconditioning.

4.2.2 Material characterizations

The crystallographic information and phase identification of the prepared materials were confirmed by room temperature X-ray diffraction (XRD) using Cu-Kα radiation (λ = 1.54 Å) operated at 40 kV and 15 mA between 2θ of 10°−80° at a scan rate of 3° per minutes. The structure was refined by the Rietveld refinement method using FULLPROF suite software. The morphological and compositional features of the sintered compounds were carried out by scanning electron microscope (EVO-Scanning Electron Microscope MA15/18) and the HR-TEM (FEI TECNAI G2 20 TWIN) operated at 300 kV equipped with EDS system. The electronic structures of the materials were studied using X-ray photoelectron spectroscopy (Thermo Scientific Multilab 2000 instrument with Al Kα radiation operated at 150 W). All of the binding energy values have been charge-corrected to the core level XPS spectra of C 1*s* located at 284.5 eV and the peak deconvolution has been done with the help of the XPSPEAK 4.1 software program. The chemical structure of materials was investigated through Raman spectroscopy, using an inVia micro-Raman

(Renishaw) spectrophotometer with an argon ion laser source having wavelength 532 nm and power 10 mW, in the wave number range of 200 to 1000 cm^{-1}.

4.2.3 Preparation of Electrode for electrochemical measurements

All the electrochemical measurements were performed using Corrtest (CS studio6) electrochemical workstation. The working electrodes were prepared by mixing the synthesized active materials ($K_{0.4}MnO_2$. xH_2O and $AgFeO_2$@C), acetylene black, and polyvinylidene difluoride (PVDF), as a binder in a weight ratio of 8:1:1 in 2 mL of N-methyl pyrrolidone (NMP), which was used as a solvent. The as-prepared homogeneous ink was drop-casted on a carbon paper substrate with mass loading ~1 mg cm^{-2} and dried at 80 °C for 12 h in a vacuum oven. The electrochemical measurements of individual working electrodes ($K_{0.4}MnO_2$. xH_2O and $AgFeO_2$@C) were performed using a three-electrode setup with a platinum wire as a counter electrode and Ag/AgCl/4M KCl as a reference electrode. The charge storage ability of both the electrodes was investigated separately, by performing cyclic voltammetry and galvanostatic charge/discharge measurements in different potential windows (0 to 1.1 V for $K_{0.4}MnO_2$. xH_2O and -1 to 0 V for $AgFeO_2$@C vs Ag/AgCl) at different scan rates and current densities in 1M Na_2SO_4 electrolyte. The full-cell ASC device was fabricated in the form of a pouch cell, by using $K_{0.4}MnO_2$. xH_2O as a cathode and $AgFeO_2$@C as an anode, and Whatman filter paper as a separator soaked in 1 M Na_2SO_4 electrolyte. The charge storage performance of as-fabricated ASC ($AgFeO_2$@C//$K_{0.4}MnO_2$. xH_2O) was investigated at different scan rates (from 5 to 100 mV sec^{-1}) and current densities (from 0.5 to 5 A g^{-1}) in 1M Na_2SO_4 electrolyte.

4.3 Results and Discussion

4.3.1 XRD study

Fig. 4.1, shows the powder X-ray diffraction (XRD) pattern of $K_{0.4}MnO_2$. xH_2O was obtained after removing the flux sources. The main phase of the obtained material is birnessite- $K_{0.4}MnO_2$. xH_2O (JCPDS No. 80-1098, monoclinic, C2/m), having a hexagonal pyramidal shape. The crystallites grown via the facile chemical flux method has a lateral dimension in the range of 2-5 μm, which is much larger than that prepared by other reported methods suggesting a superior crystal growth mechanism. It should be noted that reaction

temperature and the concentration of fluxing agent play a crucial role in the phase formation of birnessite- $K_{0.4}MnO_2$. xH_2O. At a lower temperature range of 500 to 600 °C, usually, a rod-shaped hollandite-type potassium manganese oxide has been formed, whereas when the temperature is raised to ≥700 °C, the hollandite crystal transforms to birnessite-type potassium manganese oxide. Therefore, birnessite- $K_{0.4}MnO_2$. xH_2O grows via the dissolution-deposition mechanism. The decomposition temperature of KNO_3 plays a crucial role in the phase formation of the potassium manganese oxide phase. It has been observed that, above 400 °C, KNO_3 decomposes according to the following reaction:

$$2KNO_3 \rightarrow \quad K_2O + 2NO_2 + [O]$$

At low-temperature, only a small amount of KNO_3 decomposes which may produce a little concentration of K^+ ions in the reaction mixture that may react with manganese to form the hollandite-type $K_{0.19}MnO_2$. However, when the temperature is raised, a higher amount of

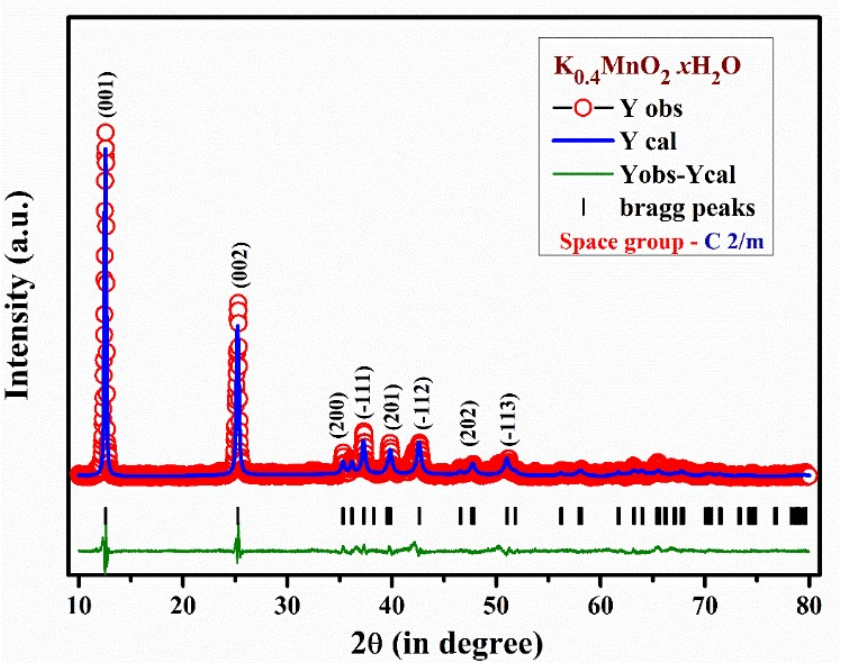

Figure 4.1: XRD pattern of as-prepared $K_{0.4}MnO_2$. xH_2O along with the Rietveld refinement study in 2Θ range of 10-80⁰

Table 4.1: Structure parameter of $K_{0.4}MnO_2$. xH_2O based on Rietiveld refinement:

$K_{0.4}MnO_2.xH_2O$						
Atoms	**x**	**y**	**z**	**Cell parameters**		**Reliability factors**
K	-0.395(6)	0.0000	0.136(3)	Bond-length	Bond angle	R_{Bragg} = 8.94
Mn	0.0000	0.0000	0.0000	a = 5.16(13)	α = 90	R_f = 7.00
O1	0.201(13)	0.0000	0.159(5)	b = 2.84(8)	β = 100.45(3)	**χ^2 = 2.38**
O2	0.718(7)	0.0000	0.522(2)	c = 7.17(19)	γ = 90	

KNO_3 is decomposed that resulting in a higher concentration of K^+ ions in the reaction mixture. At high concentrations of K^+-ions, the hollandite structure destabilizes and transforms to layered birnessite-$K_{0.4}MnO_2.xH_2O$. Further, the structural analysis of the prepared materials has been carried out by performing a Retiveld refinement study of birnessite- $K_{0.4}MnO_2.xH_2O$ and the refined crystallographic parameters are listed in Table 4.1. The low values of the goodness of fit, χ^2 suggest that refinement is quite satisfactory. The powder XRD pattern of the birnessite sample (Figure 4.1) has a monoclinic crystal structure having space group C2/m. At a lower 2θ value (< 30°) the two most intense reflections corresponding to the (001) and (002) plane of the monoclinic phase has an interlayer spacing of 0.72 and 0.32 nm respectively, whereas, at a higher 2θ value (30-80°), the other weak reflections of (200), (-111), (201), (-112), (202) and (-113) are also observed that correspond to the ordered distribution of interlayer cations along with crystal water molecules. The presence of crystal water and alkali K^+ ions stabilize the potassium manganese oxide into the birnessite lattice. All these results indicate that the synthesized birnessite- $K_{0.4}MnO_2.xH_2O$ is highly crystalline in nature and the crystallites were grown preferentially along the [00*l*] direction.

4.3.2 Thermal analysis

The amount of structured water present in the crystal is further determined by the thermal gravimetric/differential thermal gravimetric (TGA/DTG) method from 25 to 1000 °C under a nitrogen atmosphere, depicted in Figure 4.2. Most of the weight loss (~7.8%) from 25 to 200 °C is due to the evaporation of intercalated and adsorbed water. The DTG curve contained two endotherms; the first endotherm from 25 to 87 °C is attributed to the

evaporation of physically adsorbed water (2.6% by weight), while the second endotherm (at temperatures more than 87 °C) is due to the removal of lattice water (5.2% through weight), which are equivalent to 0.55 molecules of crystal water, other losses may be due to the removal of K^+ ions from the lattice at higher temperatures. Therefore, the final chemical composition of synthesized birnessite may be expressed as $K_{0.4}MnO_2$. $0.55H_2O$.

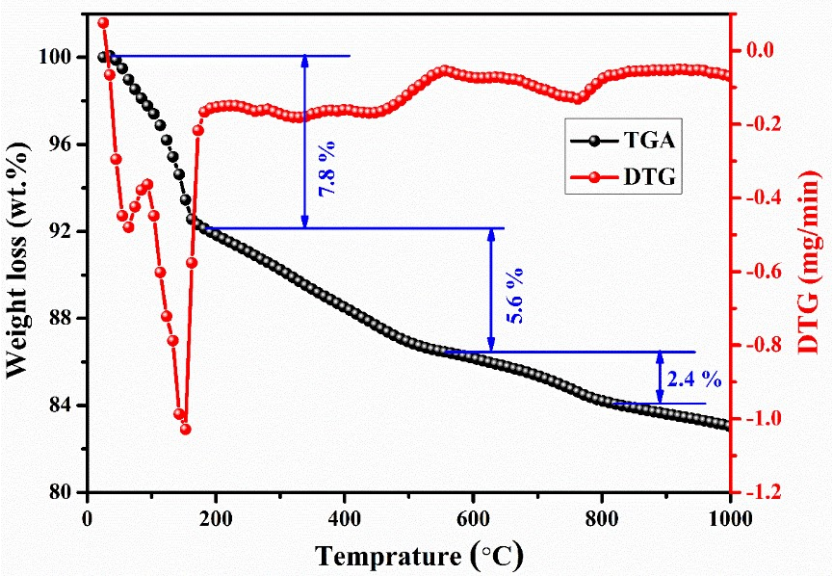

Figure 4.2: represents the TGA/DTG profile of $K_{0.4}MnO_2$. xH_2O under a nitrogen atmosphere.

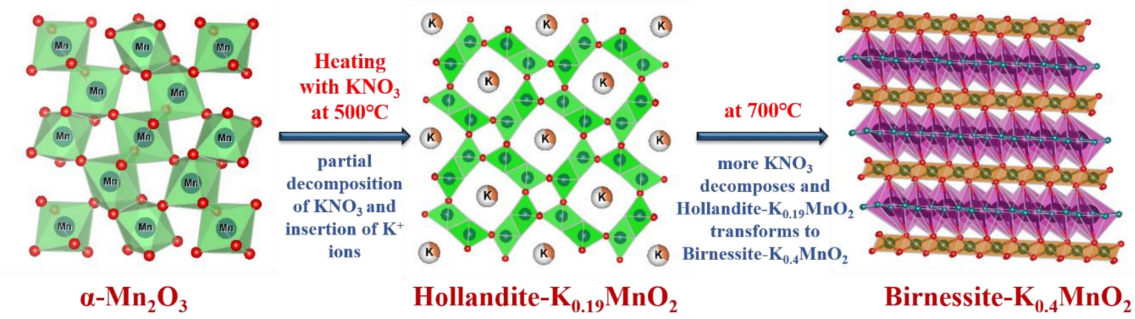

Figure 4.3: Schematic formation of birnessite-type $K_{0.4}MnO_2$. xH_2O.

The schematic formation of the birnessite-$K_{0.4}MnO_2$. xH_2O can be represented graphically in Figure 4.3. Initially, at low-temperature, only a small amount of KNO_3 is available to react with α-Mn_2O_3 for the formation of the hollandite framework (K/Mn = 0.18). Later, on raising

the temperature, the K^+ ions concentration increases, and the hollandite structure becomes unstable and transforms into a birnessite-type layered structure (K/Mn = 0.4).

4.3.3 Raman analysis

Raman analysis of the prepared material has been carried out to get a clear picture of the structural features of the birnessite-$K_{0.4}MnO_2$. xH_2O. Figure 4.4 shows the Raman spectra of birnessite- $K_{0.4}MnO_2$. xH_2O, which contains three intense peaks at ~502, ~578, and ~641 cm^{-1}, and two weak peaks nearly at 280 and 408 cm^{-1}. The variation in the peak intensities is ascribed to the difference in the growth condition. In the [MnO_6] group, the symmetric stretching vibrations of the Mn−O bond (A_{1g}) give rise to the band at 641 cm^{-1}, whereas the band at 578 cm^{-1} can be assigned to the (F_{2g}) Mn−O stretching vibration in the basal plane of [MnO_6] sheets. The band at 502 cm^{-1} can be attributed to the vibrational frequency inherent to the presence of Mn^{4+} ions. Generally, pristine MnO_2 shows Raman-shift at 500-510, 575-585, and 625-650 cm^{-1}, however, some additional peaks were also reported. Interestingly, peaks at 280 and 408 cm^{-1} can be considered as a function of modification in structure due to the insertion of alkali ions (K^+) in between the [MnO_6] basal planes [83]. For pre-insertion of the alkali metal ions, the trigonal prismatic sites in between [MnO_6] basal planes are the most accessible locations. Therefore, the peaks at 280 and 408 cm^{-1} could be assigned due to the insertion of K^+ ions in the $K_{0.4}MnO_2$. xH_2O lattice.

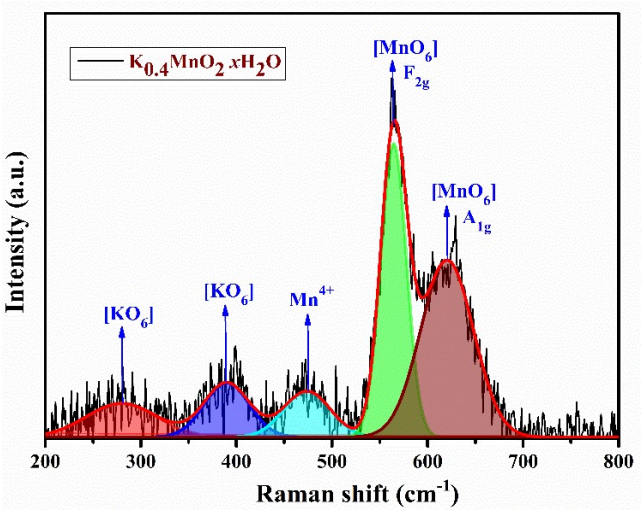

Figure 4.4: Raman spectra of as-synthesized $K_{0.4}MnO_2$. xH_2O.

4.3.4 XPS analysis

The electronic structure of $K_{0.4}MnO_2$. xH_2O are analyzed by X-ray photoelectron spectroscopy (XPS). Figure 4.5a shows the core level XPS spectra of Mn 2p that can be well-fitted to an intensive Mn^{4+} doublet accompanied by a weak Mn^{3+} doublet. Two peaks at 642.6 and 653.6 eV could be attributed to the spin-orbit doublet of Mn $2p_{3/2}$ and Mn $2p_{1/2}$, which is well consistent with the Mn^{4+} state, observed in α-MnO_2. Simultaneously, the weak peaks located at 642.1 and 656.0 eV could be assigned to the existence of Mn^{3+} in $K_{0.4}MnO_2$. xH_2O. The atomic ratio of Mn^{3+}/Mn^{4+} in the prepared birnessite is found to be 0.4. The higher ratio of the $Mn^{3+/}Mn^{4+}$ in $K_{0.4}MnO_2$. xH_2O indicates that some of the Mn^{4+} ions have been partially reduced to Mn^{3+} due to the insertion of K^+ ions into the lattice. The K/Mn ratios of the product were further confirmed by taking the core level spectra of Mn 3*s*, shown in Figure 4.5b. The spin-orbital separation of Mn 3*s* peaks equivalent to 4.85 eV, confirms that most of the Mn present in $K_{0.4}MnO_2$. xH_2O exists in the 4+ oxidation state. Figure 4.5c shows the apparent presence of K^+ (K $2p_{1/2}$ = 295.1 eV and K $2p_{3/2}$ = 292.1 eV) in $K_{0.4}MnO_2$. xH_2O, confirming that K^+ ions can be stably inserted into the α-MnO_2 [195][196][52][53]. Additionally, the O 1s spectra can be fitted into three components of 529.8, 531.4, and 532.9 eV, which correspond to Mn-O-Mn, Mn-OH, and adsorbed H_2O, depicted in Figure 4.5d, respectively. These three peaks have been chosen for the determination of mean oxidation states of Mn, according to the following formula[197]:

$$Oxidation\ state = \frac{4 \times (A_{Mn-O-Mn} - A_{Mn-OH}) + 3 \times (A_{Mn-OH})}{A_{Mn-O-Mn}} \ldots\ldots (4.1)$$

where A stands for the area under the curve of different components of core level XPS spectra of O 1*s* and by integrating the area under the curve, the average oxidation state of Mn was found to be 3.874 eV. In short, the mean oxidation state and higher spin-orbital separation of Mn 3*s* spectra confirm the formation of $K_{0.4}MnO_2$. xH_2O.

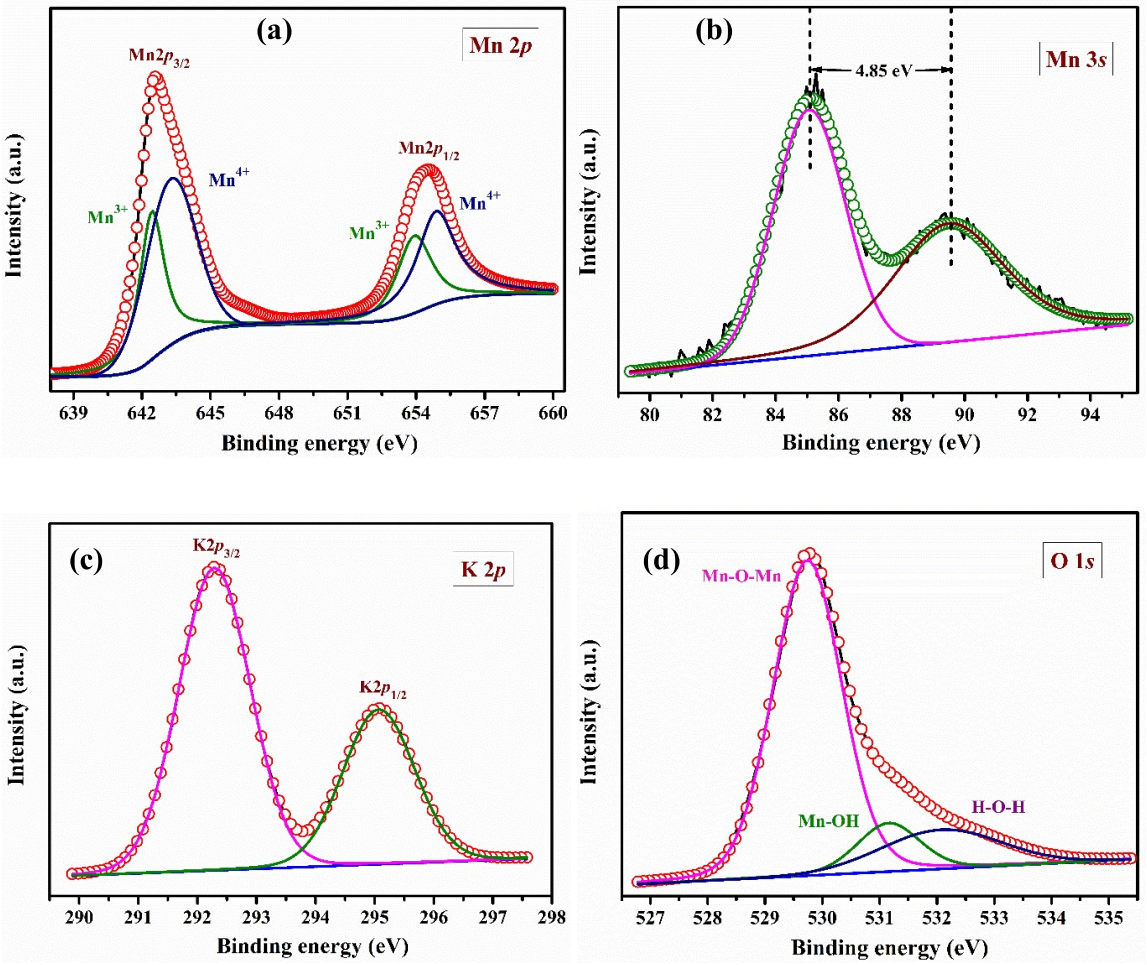

Figure 4.5: Core level XPS spectrum of (a) Mn 2p, (b) Mn 3s, (c) K 2p, and (d) O 1s.

4.3.5 Microstructural and morphological analysis

The microstructure and morphology of $K_{0.4}MnO_2$. xH_2O is determined by scanning electron microscope (SEM) and transmission electron microscope (TEM). Figure 4.6a displays the field emission scanning electron microscopy image of $K_{0.4}MnO_2$. xH_2O, which indicates that particles are hexagonal/pyramidal in shape with lateral dimensions in the range of 2-5 μm. Figure 4.6b depicts the selected region at which, color mapping of various elements viz. Mn, O, and K atoms have been carried out, which shows that each element is homogeneously distributed over the entire region of the micrograph. The energy dispersive spectra, shown below the SEM image, Figure 4.6c, confirms that the atomic ratio of K/Mn in the synthesized material is 0.4, which is in accordance with the XPS result. Further, the bright-field TEM image given in Figure 4.7a demonstrates the edge of a hexagonal sheet of

$K_{0.4}MnO_2$. xH_2O, which originated due to the strong ultrasonic treatment of the stacked sheets. The high resolution-TEM image, Fig. 4.7b & 4.7c, displays the lattice fringes corresponding to the (001) and (002) plane of monoclinic $K_{0.4}MnO_2$. xH_2O, which have inter-planar d-spacing of 0.72 and 0.32 nm, respectively. The presence of distinct diffraction spots in the selected area electron diffraction (SAED) pattern, confirms that the synthesized $K_{0.4}MnO_2$. xH_2O is highly crystalline in nature and the crystallites are grown along the [001] direction (Fig. 4.7d).

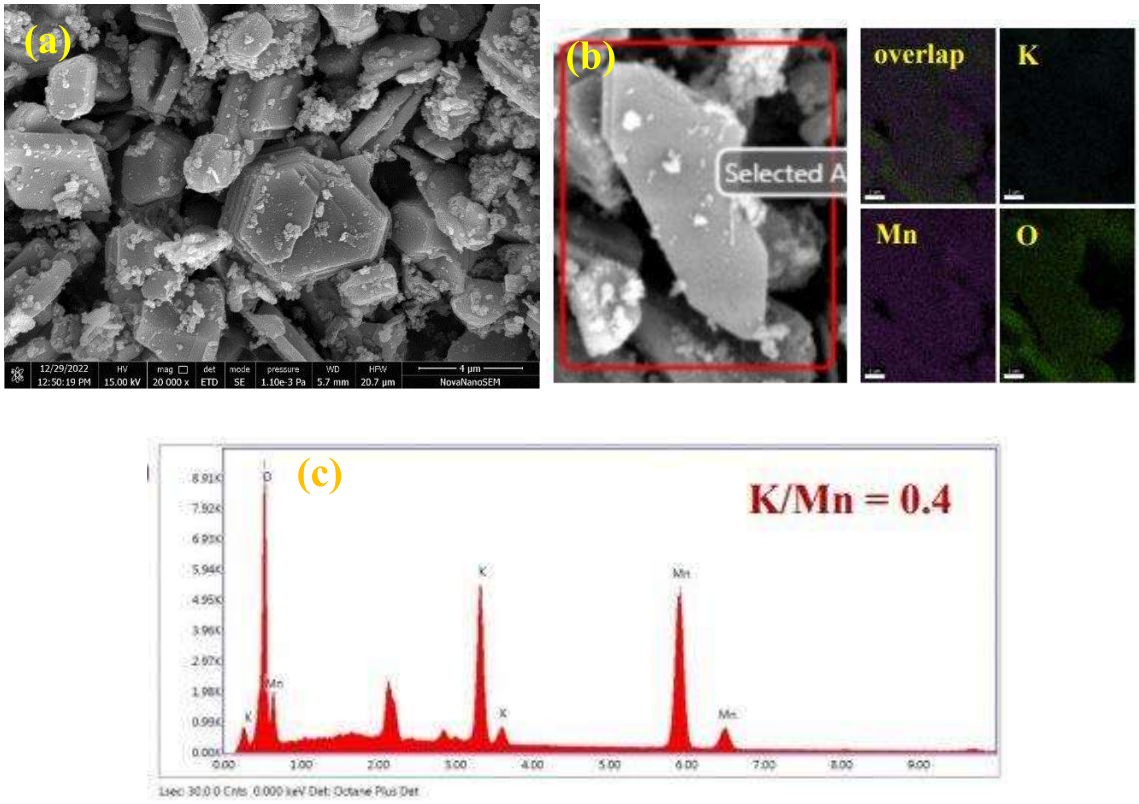

Figure 4.6: (a) SEM micrograph, (b), and (c) shows elemental color mapping and EDS spectrum of the selected area of $K_{0.4}MnO_2$. xH_2O.

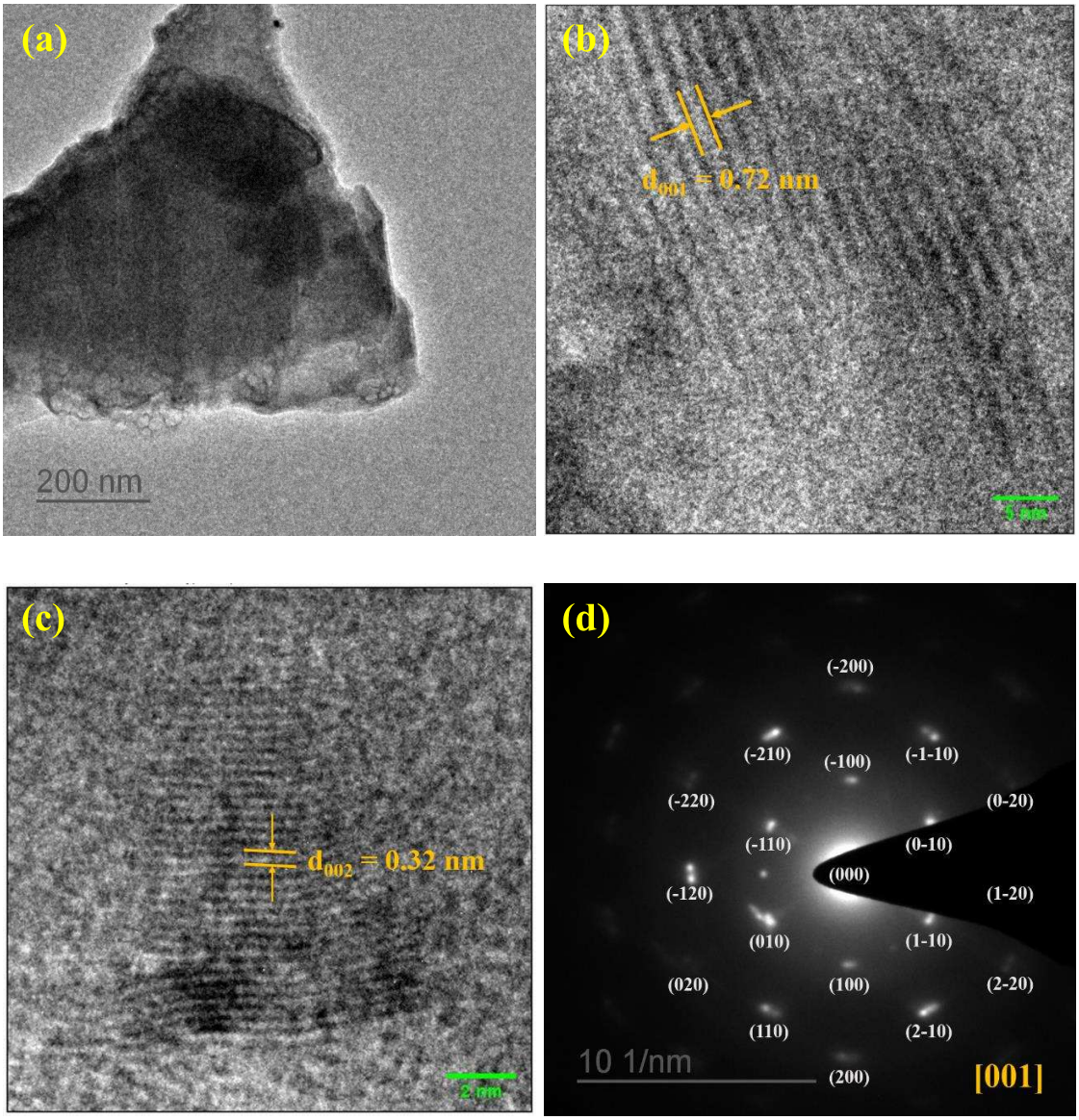

Figure 4.7: (a) the bright-field TEM image of $K_{0.4}MnO_2$. xH_2O, (b) & (c) shows the HR-TEM image with inter-planar d-spacing of (001) and (002) plane, and (d) corresponds to the SAED pattern of $K_{0.4}MnO_2$. xH_2O.

4.3.6 Surface area measurement

The porosity and the specific surface area of the prepared material have been investigated with the help of the Brunauer–Emmett–Teller (BET) surface area analyzer method. Figure 4.8 represents the nitrogen adsorption/desorption isotherms for $K_{0.4}MnO_2$. xH_2O, which confirms that the isotherm is of type II and H3 type hysteresis loop, showing a characteristic feature of a mesoporous material with a layered structure. Further, these

nanosheets are linked to each other to form the mesoporous structure with pore size distribution in the range of 10-40 nm. The specific surface area of $K_{0.4}MnO_2$. xH_2O was found to be 10 m^2 g^{-1}, which is beneficial for the fast faradaic reaction.

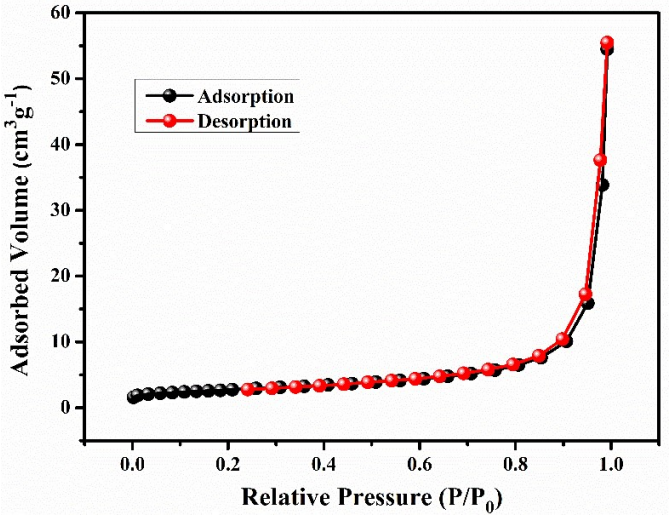

Figure 4.8: represents the N_2 adsorption/desorption isotherm of $K_{0.4}MnO_2$. xH_2O.

4.3.7 Electrochemical measurements

The electrochemical features of the layered birnessite- $K_{0.4}MnO_2$. xH_2O was investigated by recording CV curves at various scan rates from 5 mV s^{-1} to 100 mV s^{-1} in the potential window of 0-1.1 V vs Ag/AgCl, shown in Figure 4.9a. It is noted that at a scan rate of 5 mV s^{-1}, the CV curve displays a pair of redox peaks at about 0.79 V for the anodic scan and 0.59 V for the cathodic scan, which corresponds to the reversible redox reaction of $Mn^{3+/}Mn^{4+}$ accompanied with the insertion/extraction of Na^+ ions. These pairs of redox peaks were slightly shifted to higher and lower potentials on increasing the scan rates, which may be due to the polarization effect of the electrode materials. All the previously reported MnO_2-based electrodes exhibited limited charge storage performance in the narrow voltage window of 0- 0.8 or 0-1.0 V, which limits its application in high-performance ASCs. It should be observed that the operating potential window of the MnO_2-based electrode can be extended greater than 1.0 V by introducing alkali ions into the MnO_2 lattice. However, by using Ti and Ni-based-metal substrates, it is not possible to access the potential window beyond 0.8 V because it oxidizes the water molecules at a higher potential (≥ 0.8 V). In the present work,

the working potential window for the $K_{0.4}MnO_2$. xH_2O electrode can be extended up to 1.1 V by using carbon paper as a current collector, which offers new opportunities to develop high-performance ASCs. Further, we have examined the variation of the specific capacitance of $K_{0.4}MnO_2$. xH_2O electrode as a function of constant current densities from 0.5 A g^{-1} to 5 A g^{-1}, shown in Figure 4.9b. The charge-discharge profiles and the CV plots are analogous to each other and the calculated specific capacitance at various sweep rates and constant current densities are depicted in Table 4.2. To get further insight into active material, EIS analysis has been carried out at open circuit potential to evaluate the reaction kinetics and interfacial resistance of the electrode. The Nyquist plot along with its equivalent circuit model is shown in Figure 4.9c. The Nyquist plot represents the impedance characteristic as a function of applied frequency, which have three different regions: a depressed semicircle in the high-frequency region corresponding to faradaic reactions, followed by straight lines with two different slopes in the middle and low-frequency, representing the diffusion and capacitive properties of the active material respectively. Moreover, it is important to clarify the cyclic performance of material for its practical application as a supercapacitor electrode. The cyclic stability of $K_{0.4}MnO_2$. xH_2O is examined up to the 5000th cycle by applying a continuous charge/discharge current density of 10 A g^{-1} as illustrated in Figure 4.9d. The electrode exhibited 95% of its initial capacity retention after the 5000th cycle, indicating excellent stability of the as-fabricated electrode.

Table 4.2: Specific capacitance of $K_{0.4}MnO_2$. xH_2O electrode at various scan rates and current densities:

$K_{0.4}MnO_2$. xH_2O						
Cyclic voltammetry	**Scan rate (mV/s)**	**5**	**10**	**20**	**40**	**100**
	Cs (F/g)	211.68	195.21	163.95	131.16	88.57
Charge-discharge	**Current density (A/g)**	**0.5**	**1.0**	**2.0**	**3.0**	**5.0**
	Cs(F/g)	712.32	319.05	205.9	147.48	112.48

The charge storage mechanism of the $K_{0.4}MnO_2$. xH_2O electrode was further studied by performing an ex-situ XPS analysis of the electrode at various charge/discharge stages. Figure 4.10a and 4.10b displays the high-resolution XPS spectra of K 2*p* and Na 1*s* of the $K_{0.4}MnO_2$. xH_2O electrode as a function of different cycle numbers viz. pristine, 1st, 500th, and 5000th cycles. The K 2p peak of the $K_{0.4}MnO_2$. xH_2O electrode decreases with the appearance of Na 1s peak after the consecutive charge/discharge cycle as compared with the pristine case, indicating that partially K^+ ions are extracted from the host lattice with the insertion of Na^+ ions. After the 5000th charge/discharge cycle, the K 2p peak can still be observed while the Na 1s peak is clearly visible, indicating the insertion of Na^+ ions in between the layers of $K_{0.4}MnO_2$. xH_2O, which promotes the intercalating charge storage efficiency of the prepared electrode.

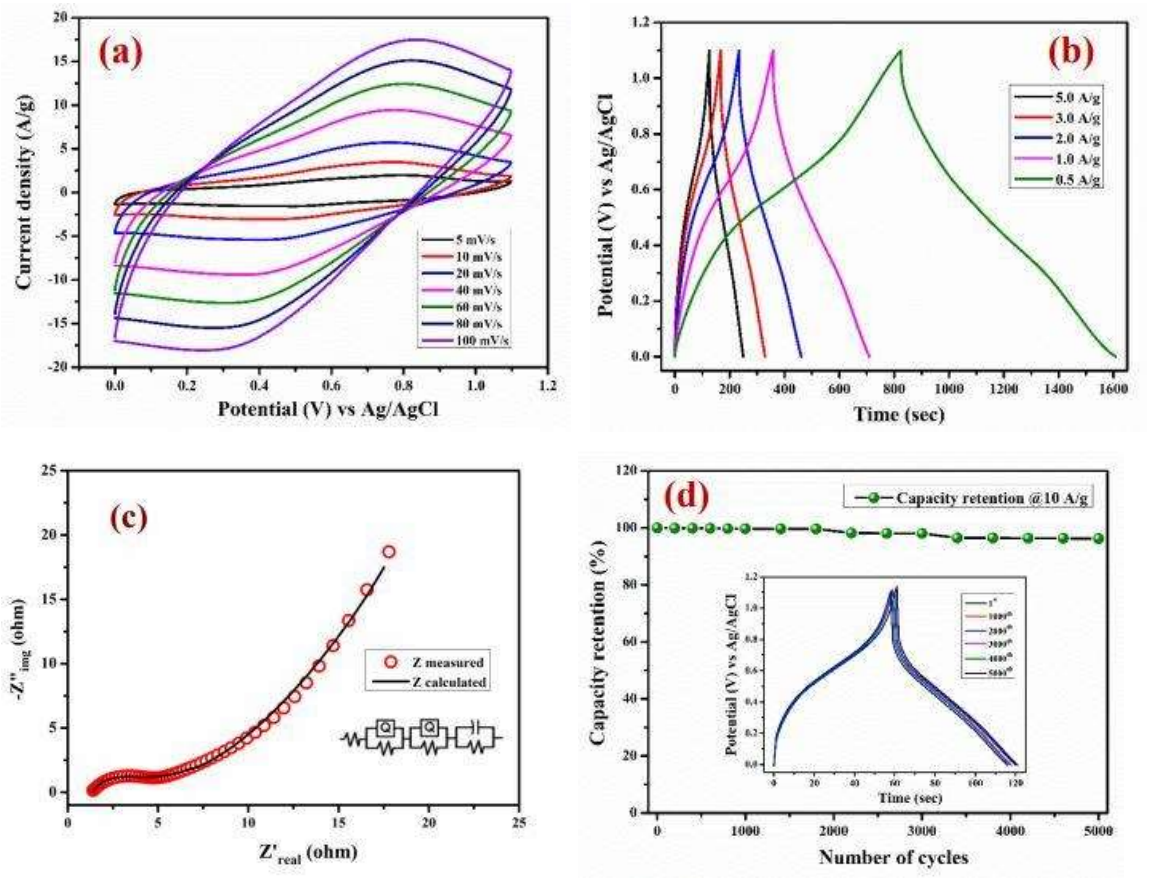

Figure 4.9: (a) CV at different scan rates starting from 5 to 100 mV s^{-1}, (b) GCD plots at different current densities from 0.5 to 5 A g^{-1}, (c) Nyquist plot at open circuit potential in the frequency range 0.1 to 100 kHz, and (d) cyclic performance at 10 A g^{-1} current density, inset show GCD curves at various time interval of $K_{0.4}MnO_2$. xH_2O electrode.

The evolution of peak intensities of K 2p and Na 1s illustrates the charge storage performance of the $K_{0.4}MnO_2$. xH_2O electrode is accompanied by extraction and insertion of Na^+ ions during the charge/discharge process, and the presence of host K^+ ions in the birnessite lattice is crucial to improve the electrochemical performance and the stability of the MnO_2 electrode. Additionally, the Mn 2p3/2 core-level XPS spectra at various applied potentials during the cathodic and anodic scan, as shown in Figures 4.10c & 4.10d demonstrates that the oxidation state of Mn changes, which is accompanied by the reversible intercalation/de-intercalation of Na^+ ions that causes the shifting of redox peak position about 0.62 eV, during the charge/discharge process.

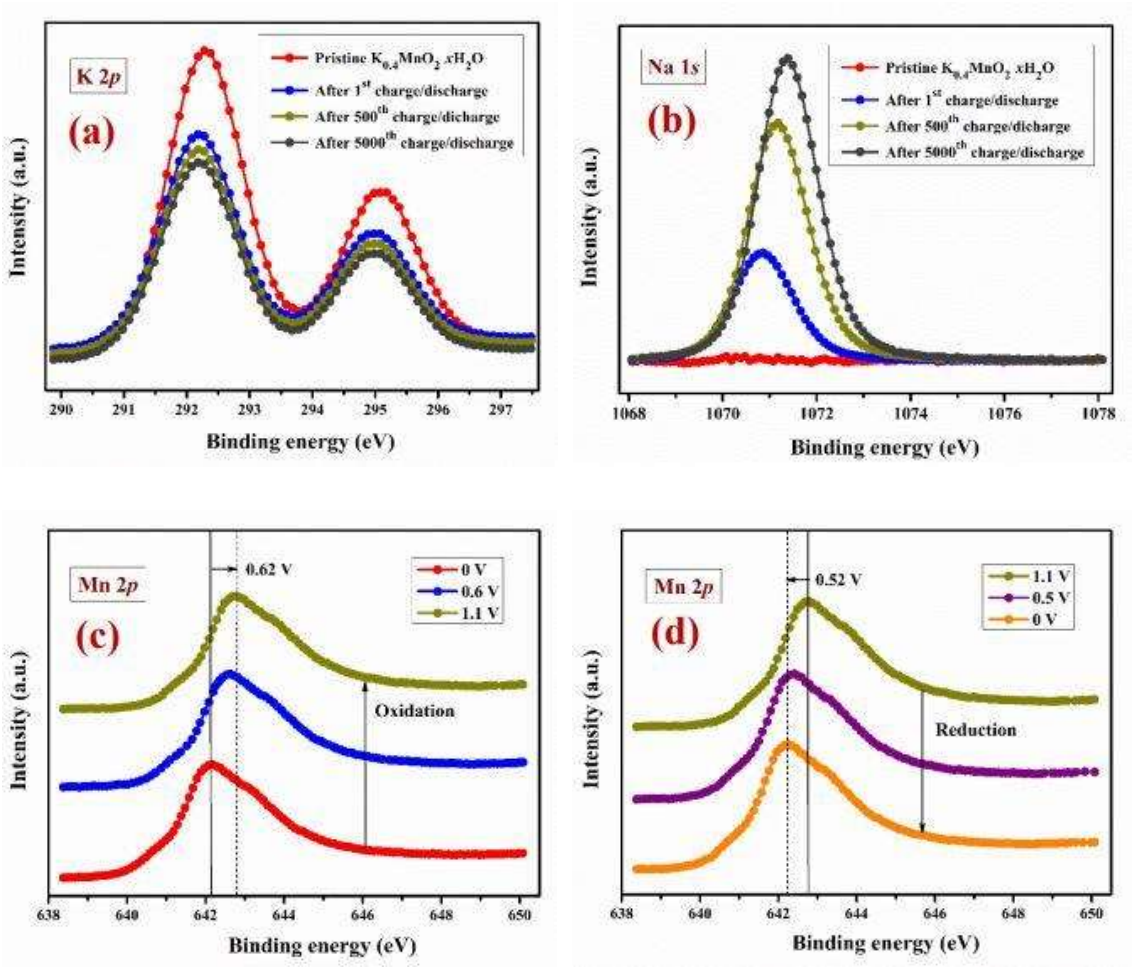

Figure 4.10: (a) K 2p, and (b) Na 1s core-level XPS spectra of the $K_{0.4}MnO_2$. xH_2O electrode at different charge-discharge states. (c) and (d) show Mn 2p3/2 core-level XPS spectra at different applied potentials during the cathodic and anodic scans.

A post-analysis of the used electrode has also been carried out to see the effect of electrochemical cycling on the microstructure of $K_{0.4}MnO_2$. xH_2O. The sample was recovered through the ultrasonic treatment of the coated electrode after the stability test. A comparison of the SEM image of spent and fresh $K_{0.4}MnO_2$. xH_2O, given in Figures 4.11a & 4.11b, confirms that there is no change in morphology and chemical composition, only the electrolyte ions are attached properly to the electrode surface.

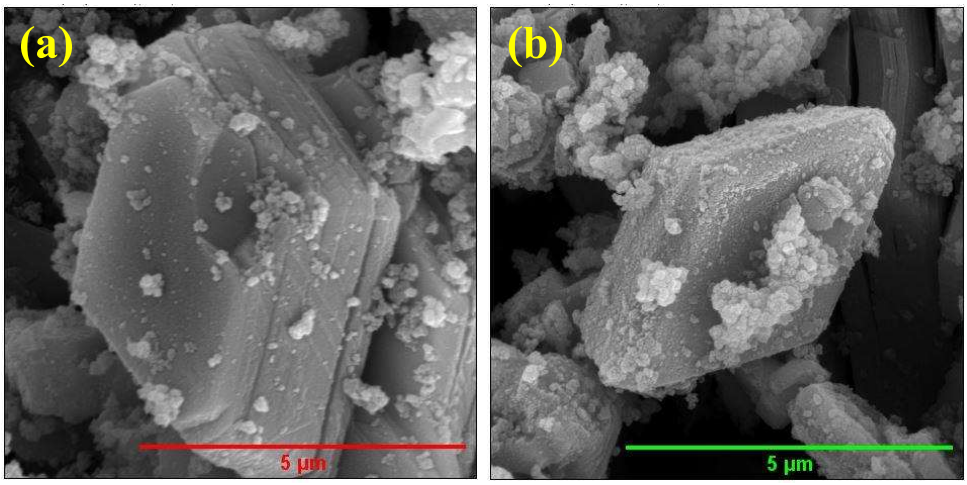

Figure 4.11: SEM micrograph of $K_{0.4}MnO_2$. xH_2O electrode (a) before and (b) after electrochemical cycling.

4.3.8 Electrochemical kinetics

The total charge stored at the electrode during supercapacitor action is dependent on (i) the faradaic contribution (i.e., pseudocapacitance), which is accompanied by the intercalation/deintercalation of Na^+ ions through the surface redox reaction and (ii) the non-faradaic contribution from the electrical double layer (i.e., EDL capacitance) that originates due to the adsorption/desorption of electrolyte ions at the electrode surface. Therefore, the former process is the result of the diffusion of electrolytic ions (e.g., Na^+, Li^+, K^+, or H^+) into the lattice, and is considered a diffusion-controlled process. The rate of charge transfer of faradaic reactions (I_F) is proportional to the square root of the scan rate (v) according to the following equation:

$$I_F = 0.495\, nFAc \left(\frac{nF\nu\alpha D_{Na^+}}{RT}\right)^{1/2} \quad \ldots\ldots (4.2)$$

where n is the number of electrons involved in the faradaic reaction, A is the surface area of the electrode materials, F is Faraday's constant, c is the concentration of electrolyte ions (e.g., Na^+) in the accumulating layer, α is the charge transfer coefficient, D is the diffusion coefficient, R is the molar gas constant, and T is the temperature. On the other hand, the double-layer capacitive current in non-faradaic regions (I_{NF}) is directly proportional to the scan rate according to the equation:

$$I_{NF} = AC_d\nu \ldots\ldots (4.3)$$

where C_d is the double-layer capacitance and A is a constant.

Therefore, at higher scan rates, the current response is mainly due to the EDL mechanism, whereas at lower scan rates, the current response is dominated by the pseudocapacitive mechanism. So, the overall current (i) is described by a simple power law:

$$i = a\nu^b \ldots\ldots (4.4)$$

$$\log i = b \log \upsilon + \log a \ldots\ldots (4.5)$$

where a is an adjustable parameter and b value lies between 0.5 to 1, representing current as a combination of both pseudocapacitance and EDL mechanism. Figure 4.12a shows the log(i) vs log(υ) plot for the $K_{0.4}MnO_2$. xH_2O electrode at the peak potentials, and the slope of the straight line gives the value of b which is found to be 0.73 for the oxidation peak and 0.72 for the reduction peak. Figure 4.12b shows the plot of b-values vs applied potential for both anodic and cathodic scans from 0.3 to 1 V (vs Ag/AgCl). In the potential window between 0.3 to 1 V for cathodic scans, the b-values were in the range of 0.7-0.85 and reached the lowest value (0.72) at around 0.6 V. These data indicate that at a lower potential, the cathodic current is a result of intercalation of Na^+ into the $K_{0.4}MnO_2$. xH_2O lattice, although the contribution from the non-faradaic component (EDL capacitance) existed throughout the operation since the b-values are always found to be greater than 0.5. These results are not similar to the alkali ions (Na^+ or K^+) intercalated δ-MnO_2 systems and are in good agreement with the similar work on Li^+ -intercalated TiO_2 for supercapacitor applications. Similarly, the b-values for anodic scan were lies in the range of 0.85-0.7 between 1 to 0.3 V, and rapidly reached the lowest value (0.73) at the potential of 0.8 V. These data also suggested that at

higher potential, the anodic currents arose primarily from faradaic reactions through the extraction of Na^+ from the $K_{0.4}MnO_2.xH_2O$ lattice.

So, at a given potential the current response (i) is a combination of two separate mechanisms, namely, pseudo (faradaic) and EDL (non-faradaic), and governed by the following equation:

$$i = k_1\nu + k_2\nu^{1/2} \dots\dots (4.6)$$

This can be further modified as

$$\frac{i(V)}{\upsilon^{1/2}} = k_1\upsilon^{1/2} + k_2 \dots\dots (4.7)$$

where $k_1\,\upsilon$ and $k_2\,\upsilon^{1/2}$ correspond to the capacitance contributions from the surface-controlled process and diffusion-controlled processes, respectively. Thus, by determining the values of slope and intercept of the plot $i/\upsilon^{1/2}$ between $\upsilon^{1/2}$ and, shown in Figure 4.12c, we can distinguish the surface-controlled and diffusion-controlled process of $K_{0.4}MnO_2.xH_2O$ electrode, separately. Figure 4.12d represents the CV curve of $K_{0.4}MnO_2.xH_2O$ showing surface-controlled contribution (pink area) and diffusion-controlled contribution (cyan area) at 5 mV $s^{-1.}$ The percentage of capacitance that is contributed by the surface-controlled process of $K_{0.4}MnO_2.xH_2O$ is 57%, 66%, 73%, 79%, 83%, 88%, and 92% at scan rates of 5, 10, 20, 40, 60, 80, and 100 mV s^{-1}, respectively shown in Fig. 4.12e. However, the capacitance contribution of the diffusion-controlled process progressively decreases with the growing scan rate, because, at a higher scan rate the inner part of the electrode has a negligible contribution to the redox reaction.

Further, the charge contribution at the inner and outer surface of the electrode can be quantified separately using a Trasatti plot. Figures 4.12f & 4.12g show the Trasatti plot of the $K_{0.4}MnO_2.xH_2O$ electrode. The y-intercept of the linear fit of q^{-1} vs $\upsilon^{1/2}$ at $\upsilon = 0$ represents the total amount of charge stored (including inner and outer surface) at the electrode (Fig. 4.12g), whereas, the y-intercept of the linear fit of q vs $\upsilon^{-1/2}$ at $\upsilon = 0$ shows the charge stored only at the outer surface of the electrode (Fig. 4.12f). So, the charge storage contribution for inner electrode surface can be quantified mathematically, as Q_{total} - Q_{out}. According to the Trasatti plot for $K_{0.4}MnO_2.xH_2O$, Q_{out}, and Q_{in} are found to be 74 and 332 C g^{-1} respectively.

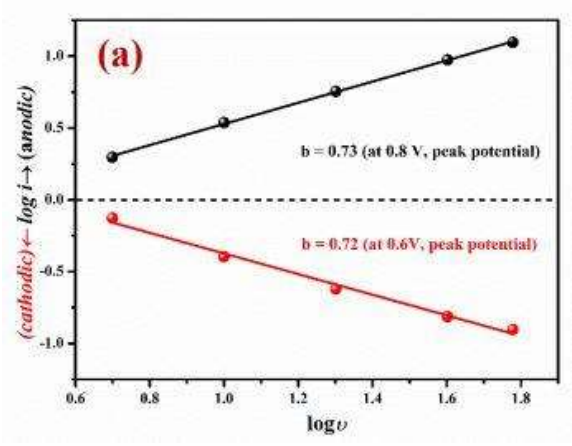
(a)
b = 0.73 (at 0.8 V, peak potential)
b = 0.72 (at 0.6V, peak potential)
(cathodic)← log i→ (anodic)
logυ

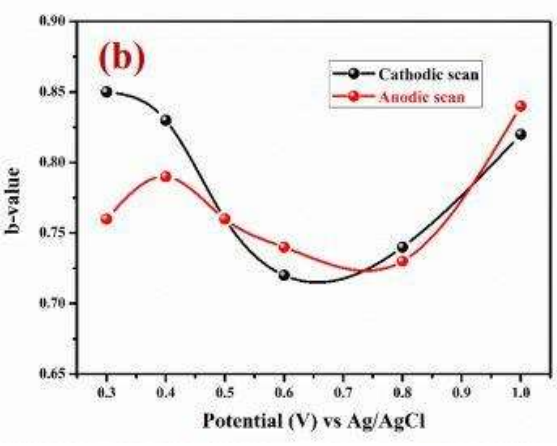
(b)
Cathodic scan
Anodic scan
b-value
Potential (V) vs Ag/AgCl

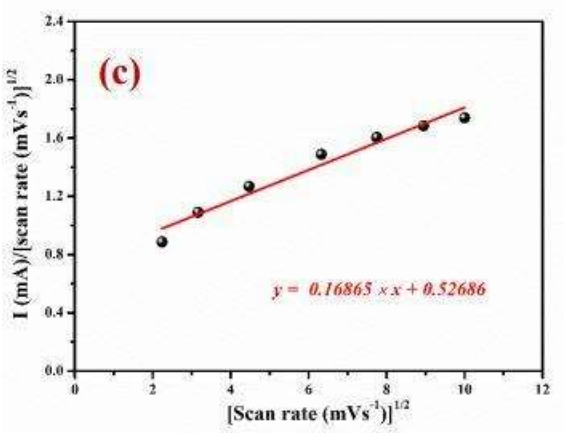
(c)
y = 0.16865 x x + 0.52686
I (mA)/[scan rate (mVs-1)]1/2
[Scan rate (mVs-1)]1/2

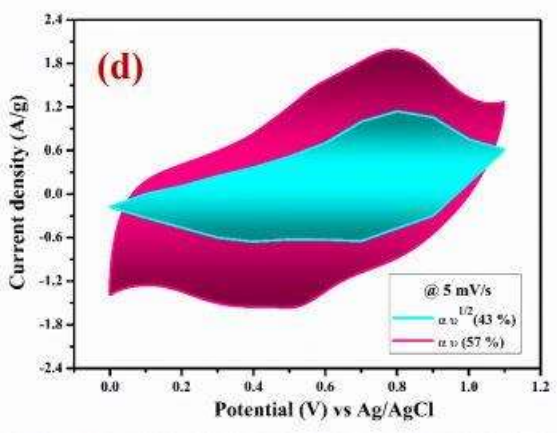
(d)
@ 5 mV/s
α υ1/2 (43 %)
α υ (57 %)
Current density (A/g)
Potential (V) vs Ag/AgCl

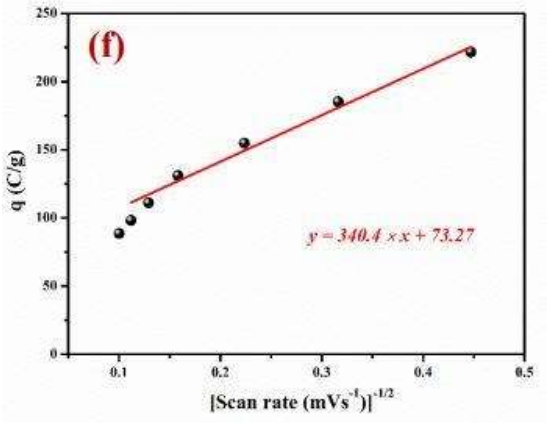
(f)
y = 340.4 x x + 73.27
q (C/g)
[Scan rate (mVs-1)]-1/2

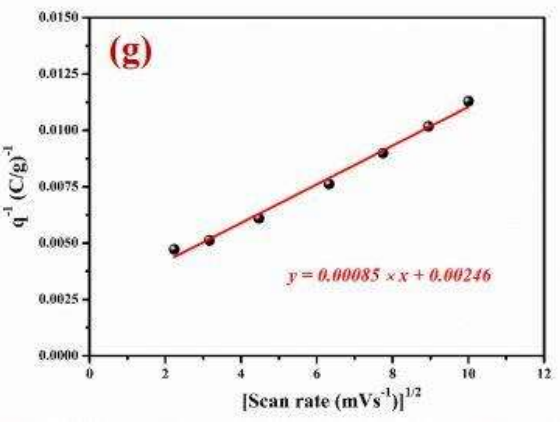
(g)
y = 0.00085 x x + 0.00246
q-1 (C/g)-1
[Scan rate (mVs-1)]1/2

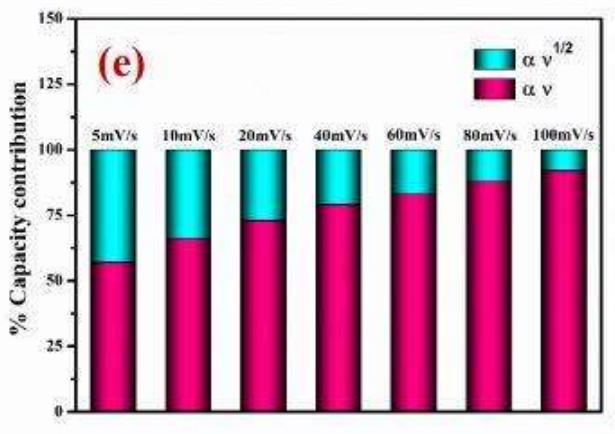

Figure 4.12: (a) log i_{cp}, log i_{ap} vs log υ plot, (b) variation of b with applied potential, (c) plot between $i/\upsilon^{1/2}$ vs. $\upsilon^{1/2}$, (d) CV at 5 mV s^{-1} showing intercalation and surface contribution separately, (e) intercalation and surface contribution at different scan rate, and (f and g) corresponds to the Trasatti plot of $K_{0.4}MnO_2$. xH_2O electrode.

4.3.9 Full-cell asymmetric ($AgFeO_2$@C//$K_{0.4}MnO_2$. xH_2O) testing:

To determine the practical application of $K_{0.4}MnO_2$. xH_2O electrode in energy storage devices, an asymmetric cell (ASC) was fabricated using $K_{0.4}MnO_2$. xH_2O as a positive electrode (cathode) and AgFeO2@C as a negative electrode (anode) using an aqueous 1M Na_2SO_4 electrolyte. Our previous work demonstrated that silver-iron containing delafossite exhibited large specific capacitance in a large negative potential window of -1 to 0 V. However, the poor cyclic performance of the iron oxide electrode seriously limits its application in the supercapacitor field. Therefore, in the present work, an ultrathin coating of the carbon layer has been carried out to improve the cyclic stability of the $AgFeO_2$ electrode. Fig. 4.13(a) shows the Rietveld refinement XRD pattern of the $AgFeO_2$@C, which confirms that the $AgFeO_2$ has been formed into the mix phase of 2H (hexagonal) and 3R (rhombohedral). Further, the presence of D and G bands in the Raman spectrum of $AgFeO_2$@C (Figure 4.13b) indicates a high degree of carbonization in the prepared material. Additionally, the SEM image of $AgFeO_2$@C (Figure 4.13c) also confirms the successful wrapping of the carbon protecting layer on $AgFeO_2$ nanoparticles. It was noted that $AgFeO_2$@C exhibited a reduction peak at -0.9 V and an oxidation peak at -0.8 V, which corresponds to the Fe^{2+}/Fe^{3+} redox couple during the reversible electrochemical reaction. Moreover, the $AgFeO_2$@C electrode also exhibited excellent cyclic stability with 88%

capacitance retention after 5000th charge/discharge cycles at 10 A g^{-1} current density (Figure 4.13d), making it the suitable anode to couple with $K_{0.4}MnO_2$. xH_2O cathode for constructing ASC. Therefore, improvement in the capacity is a result of the carbon protection, which helps to slow down the capacity fading of the $AgFeO_2$@C electrode. Figure 4.14a shows the individual CV curves of the $K_{0.4}MnO_2$. xH_2O and $AgFeO_2$@C electrodes in separate potential windows of 0 to 1.1 V and -1 to 0 V vs Ag/AgCl at a scan rate of 20 mV s^{-1}, respectively. The operating voltage window of any ASC is highly dependent on the difference in the work function of the cathode and anode, the greater the difference in the work function wider will be the operating window. The work function of Fe_2O_3 (5.68 eV) is greater than that of MnO_2 (4.4 eV). Whenever K^+ is inserted in MnO_2, the mean oxidation state of Mn-atom changes that shifted the work function of MnO_2 towards the lower value, which results in further enlargement of the voltage window. Depending upon the charge storage performance of the cathode and anode in the separate potential window, the fabricated asymmetric device theoretically can be operated up to 2.1 V, however, in the present study we can get only a 1.8 V working potential window for this ASC device. Figure 4.14b displays the CV curves of the as-fabricated ($AgFeO_2$@C//$K_{0.4}MnO_2$. xH_2O) ASC at various scan rates from 5 to 100 mV s^{-1}. The CV curves maintained their rectangular shape at the high scan rate, indicating excellent fast charge/discharge performance of the ASC. Further, the extraordinary capacitive feature of the fabricated battery-type supercapacitive ASC was confirmed by charge/discharge measurements depicted in Figure 4.14c at various constant current densities (0.5 to 5 A g^{-1}) between 0 to 1.8 V. Table 4.3 demonstrates the specific capacitances of the battery-type supercapacitive ASC, as a function of the scan rates and current densities. At a current density of 1 A g^{-1}, the $AgFeO_2$@C// $K_{0.4}MnO_2$. xH_2O ASC exhibited a specific capacitance of 50.31 F g^{-1}, whereas when the current density was increased to 5 A g^{-1}, the fabricated battery-type supercapacitive ASC still maintained its capacitance to 13.34 F g^{-1}, which is much larger than recently developed MnO_2-based supercapacitor devices. The coulombic efficiency of the ASC device was also calculated with the help of GCD curves and it was found to be about 92% at a current density of 0.5 A g^{-1}. A slight irreversible capacitance loss could be attributed to the oxidation of water in an aqueous electrolyte at a higher voltage.

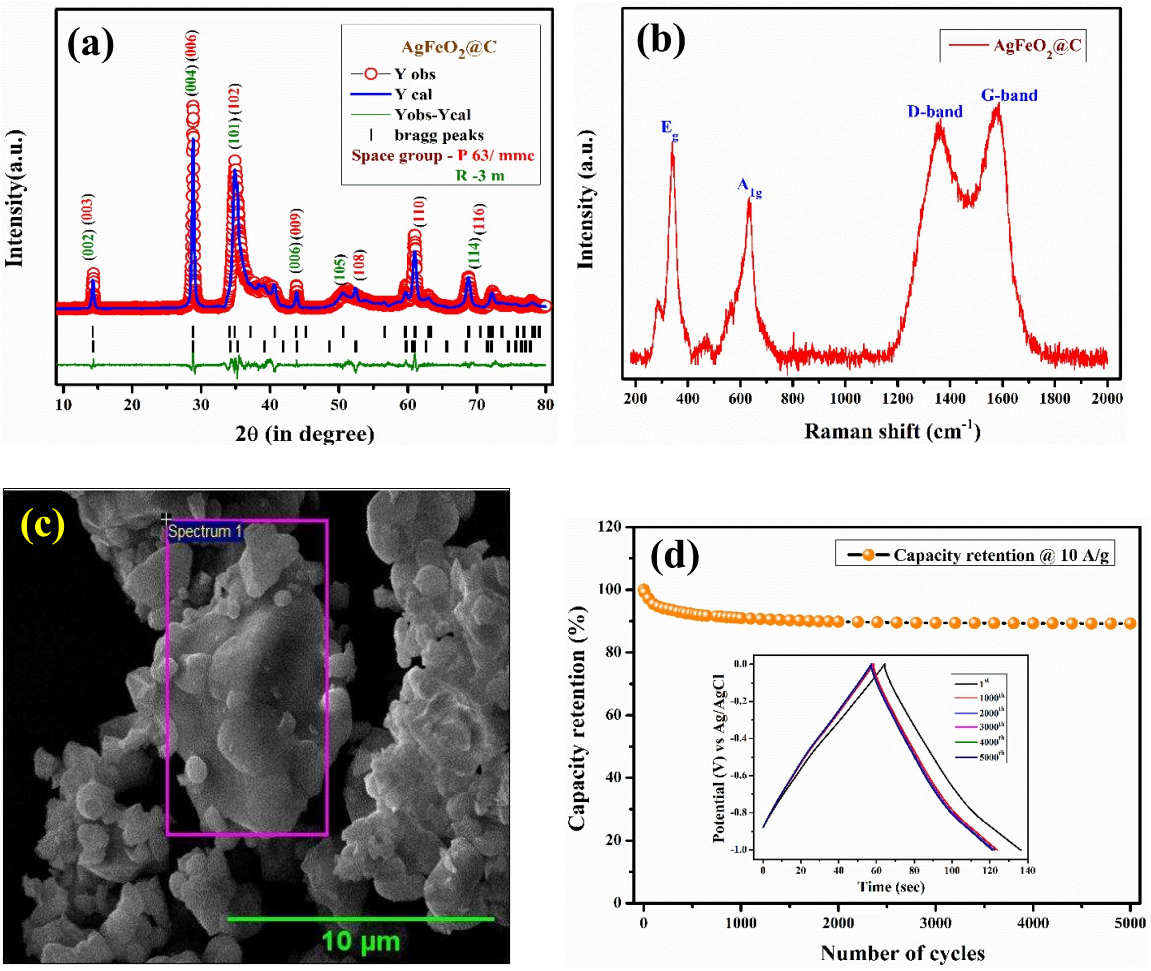

Figure 4.13: represents (a) the Rietveld refinement XRD pattern of $AgFeO_2$@C in 2Θ range 10-80⁰, (b) Raman spectra of $AgFeO_2$@C, (c) SEM micrograph of $AgFeO_2$@C, and (d) cyclic performance at 10 A g^{-1} current density, inset show GCD curves at various time interval of $AgFeO_2$@C electrode.

Based on the charge/discharge profiles at various current densities, the energy densities and power densities for the ($AgFeO_2$@C// $K_{0.4}MnO_2$. xH_2O) battery-type supercapacitive ASC were calculated and shown in the Ragone plots, Figure 4.14d. In addition to large specific capacitance and high cell voltage, the presented battery-type supercapacitive ASC can deliver an energy density equivalent to 61.51 Wh kg^{-1} and a power density of 450 W kg^{-1} at a current density of 0.5 A g^{-1}, which is substantially larger than the previously reported aqueous based asymmetric supercapacitor devices. Table 4.4 demonstrates the comparison of recently developed aqueous-based asymmetric supercapacitor devices with the presented ASC. Even at a high-power density of 2253 W kg^{-1}, the battery-type supercapacitive ASC

was able to deliver an energy density of about 6.02 Wh kg^{-1}, demonstrating superior power capability.

Table 4.3: Specific capacitance of $AgFeO_2$@C//$K_{0.4}MnO_2$. xH_2O ASC electrode at various scan rates and current densities.

$AgFeO_2$@C // $K_{0.4}MnO_2$. xH_2O						
Cyclic voltammetry	**Scan rate (mV/s)**	**5**	**10**	**20**	**40**	**100**
	Cs (F/g)	53.40	46.12	39.24	33.09	26.34
Charge-discharge	**Current density (A/g)**	**0.5**	**1.0**	**2.0**	**3.0**	**5.0**
	Cs(F/g)	136.69	50.31	27.87	18.37	13.34

Apart from the outstanding power capability, the battery-type supercapacitive ASC also exhibited excellent cyclic stability in such a large voltage window of 0-1.8 V. Figure 4.14.e, demonstrates the capacitance retention of the $AgFeO_2$@C//$K_{0.4}MnO_2$. xH_2O ASC as a function of cycle number for 5000^{th} charge/discharge cycles and the inset show the GCD curves recorded at various time intervals, at a current density of 5 A g^{-1}. After 5000^{th} consecutive cycles, about 83% of its initial capacitance was retained, indicating excellent stability of the battery-type supercapacitive ASC. Figure 4.14f depicts the Nyquist plots of the ASC recorded before and after the cyclic test, which showed a negligible change in charge transfer resistance, suggesting fast faradaic reaction occurs at both electrodes during the charge/discharge. Furthermore, to show the practical application of the $AgFeO_2$@C// $K_{0.4}MnO_2$. xH_2O battery type supercapacitive ASC, the prototype device was connected to a 1.5 V green light emitting diode (LED) and successfully lightened, shown as an inset of Figure 4.14d. The remarkable capacitive performance of the newly developed 1.8 V ASC device was schematically elaborated and presented graphically in Figure 4.15, displaying a smart device fabrication technique using an ABO_2-type pseudocapacitive electrode.

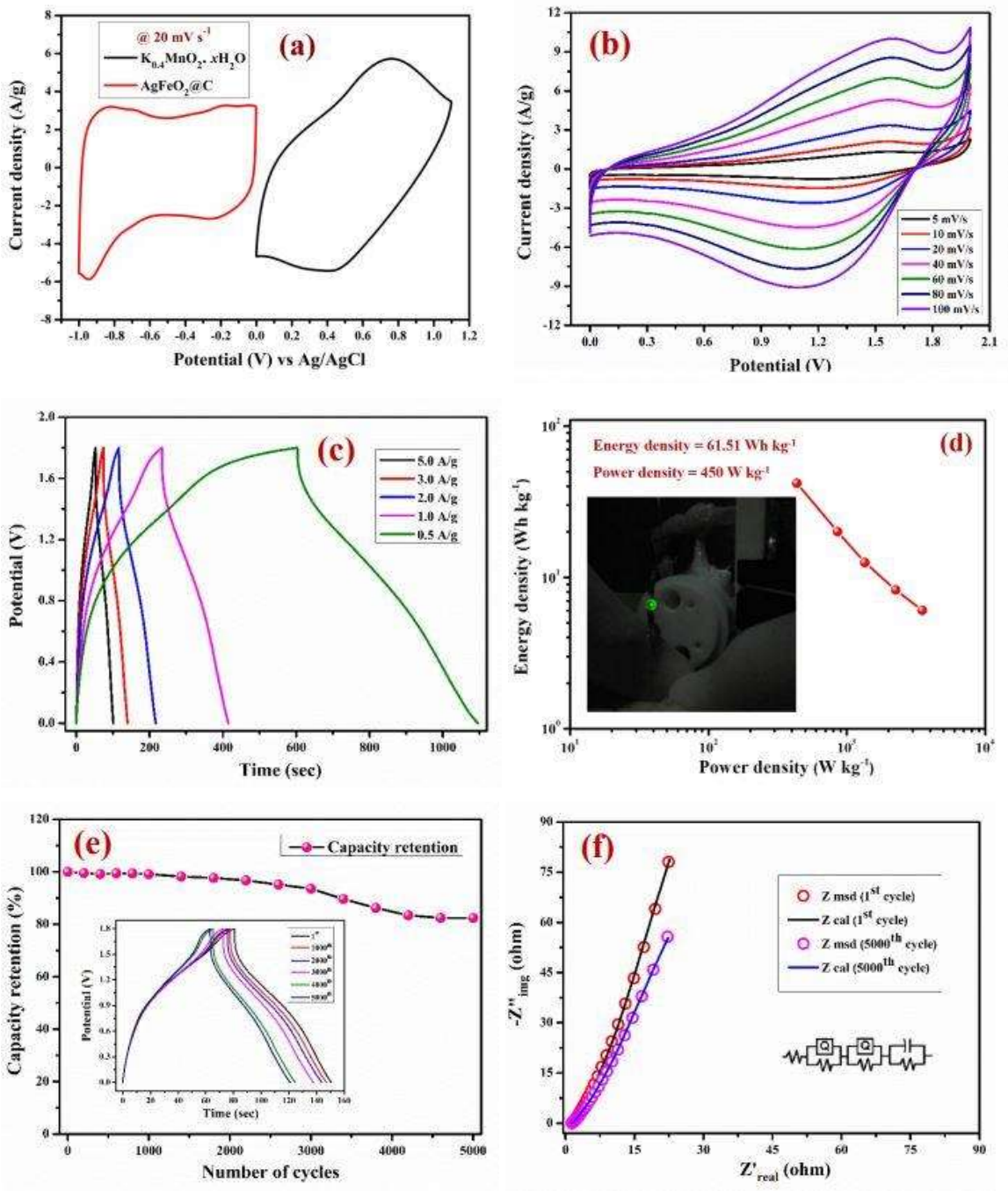

Figure 4.14: (a) individual CV curves of $K_{0.4}MnO_2.xH_2O$ and $AgFeO_2$@C electrodes in a three-electrode cell at 20 mV s^{-1} scan rate, (b) CV curves of $AgFeO_2$@C// $K_{0.4}MnO_2.xH_2O$ ASC recorded as a function of scan rates, (c) charge/discharge profile at different current densities, (d) Ragone plot of ASC device and inset show glowing of 1.5 V LED, (e) cyclic performance of ASC cell at 5 A g^{-1} current density up to 5000th cycles, and (f) Nyquist plots of ASC cell recorded before 1st and after 5000th cycles.

Table 4.4: Comparison of the electrochemical performance of previously reported MnO_2-based asymmetric supercapacitor devices with the present work:

Asymmetric device	Electrolyte	Current density ($A\ g^{-1}$)	Potential window (V)	Energy density ($Wh\ kg^{-1}$)	Power density ($W\ kg^{-1}$)
MnO_2//AC	1 M Na_2SO_4	0.5	2	40	500
MnO_2-CNT//AC	0.5 M Na_2SO_4	1.0	2	27	-
Ag-MnO_2//AC	1 M Na_2SO_4	2	2	54	2000
Fe-MnO_2//AC	1 M Na_2SO_4	0.5	2	40	250
Co_3O_4/MnO_2//AC	1 M Na_2SO_4	2	2.4	46.2	-
PANI-MnO_2//AC	6M KOH	0.5	1.6	20	400
MnO_2//Fe_3O_4	21M LiTFSI	0.1	2.2	35.5	159
MnO_2// FeOOH	1 M Li_2SO_4	4	1.85	12	3700
$Na_{0.5}MnO_2$//Fe_3O_4@C	1 M Na_2SO_4	0.5	2.6	81	647
$K_{0.4}MnO_2$. xH_2O//$AgFeO_2$@C	**1 M Na_2SO_4**	**0.5**	**1.8**	**61.51**	**450**

4.4 Conclusion

In summary, crystallites of $K_{0.4}MnO_2$. xH_2O were successfully grown via a facile chemical flux method that gives a birnessite-type layered structure having a lateral dimension in the range of 2-5 μm. Further, the insertion of K^+ ions into birnessite MnO_2 lattice not only increases the inter-layer separation of [MnO_6] octahedral of about 0.72 nm but also increases the amount of Mn^{3+} ions that supports the interconversion of Mn^{3+}/Mn^{4+} redox couple during the electrochemical reaction. The thin carbon layer coated $AgFeO_2$ electrode suppresses the dissolution of iron into the electrolyte which results in the excellent stability of the $AgFeO_2$ electrode in such a large negative potential window of 0 to -1 V. Furthermore, the protection of the carbon layer, also provides a large overpotential for hydrogen evolution, making the anode more efficient to work in the large negative potential window. Thus, the incorporation of birnessite- $K_{0.4}MnO_2$. xH_2O as a positive electrode (cathode), and the thin carbon layer coated $AgFeO_2$ as a negative electrode (anode) in aqueous 1M Na_2SO_4 electrolyte in the form of battery-type supercapacitive ASC exhibited high energy density as well as power density with excellent cycle life with cell voltages close to 2 V. Thus, the newly developed high-voltage aqueous asymmetric battery-type supercapacitive cell has a low-cost and enviro-friendly, that can replace currently market-available hazardous lead-acid batteries for fast energy storage applications. The presented battery-type supercapacitive ASC can deliver an energy density equivalent to 61.51 Wh kg^{-1} and a power density of 450.04 W kg^{-1} at a current density of 0.5 A g^{-1}, which is substantially larger than the previously reported aqueous electrolyte-based asymmetric supercapacitor devices.

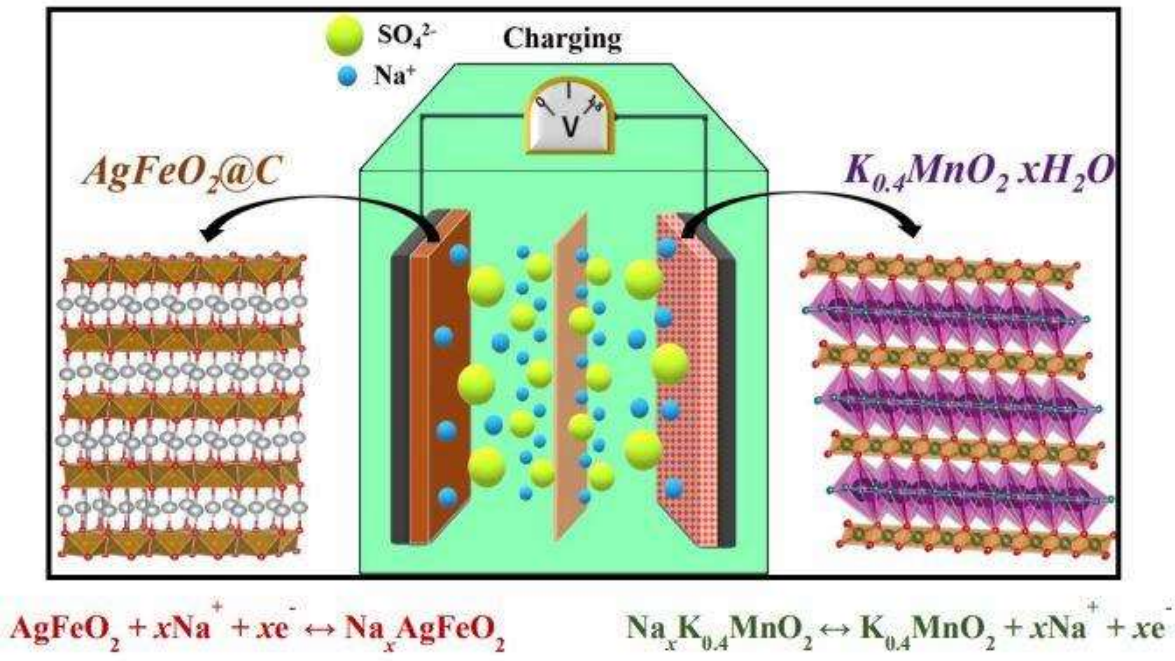

Figure 4.15: represents the device fabrication and charge-storage mechanism of the $AgFeO_2$@C anode and the $K_{0.4}MnO_2.xH_2O$ cathode in the present ASC system.